This is the accepted manuscript made available via CHORUS. The article has been published as:

Giant magnetoelastic spin-flop with magnetocrystalline instability in La_{1.4}Sr_{1.6}Mn_{2}O_{7}

K.-T. Ko, H. Jang, D.-H. Kim, B.-G. Park, J.-Y. Kim, S. B. Kim, Y.-S. Oh, S.-W. Cheong, and J.-H. Park

Phys. Rev. Materials **2**, 014408 — Published 16 January 2018

DOI: 10.1103/PhysRevMaterials.2.014408

Giant magnetoelastic spin-flop with magnetocrystalline instability in $La_{1.4}Sr_{1.6}Mn_2O_7$

K.-T. Ko,[1,2,*] H. Jang,[2] D.-H. Kim,[1,2] B.-G. Park,[3] J.-Y. Kim,[3]
S. B. Kim,[4,5] Y.-S. Oh,[6] S-W. Cheong,[5,6] and J.-H. Park[1,2,7,†]

[1] *Max Planck POSTECH Center for Complex Phase Materials, Pohang University of Science and Technology, Pohang 37673, Korea.*
[2] *Department of Physics, Pohang University of Science and Technology, Pohang 37673, Korea.*
[3] *Pohang Accelerator Laboratory, Pohang University of Science and Technology, Pohang 37673, Korea.*
[4] *Advancement for College Education Center, Konyang University, Chungnam 32992, Korea.*
[5] *l_PEM & Department of Physics, Pohang University of Science and Technology, Pohang 37673, Korea.*
[6] *R-CEM & Department of Physics and Astronomy, Rutgers University, Piscataway, NJ 08854, USA.*
[7] *Division of Advanced Materials Science, Pohang University of Science and Technology, Pohang 37673, Korea.*

We studied a low-field giant magnetostrictive spin-flop transition in a colossal magnetoresistance manganite $La_{1.4}Sr_{1.6}Mn_2O_7$ using resonant soft x-ray diffraction and soft x-ray absorption spectroscopy at the Mn $L_{2,3}$-edge. The spin-flop transition is induced by an instability of magnetoscrystalline anisotropy near a critical e_g orbital configuration with a balanced occupation in $d_{x^2-y^2}$ and $d_{3z^2-r^2}$ states, which contribute in-plane and out-of-plane orbital angular momenta, respectively. The magnetic field drives a certain change in the orbital occupation with lattice distortion to switch the magnetic anisotropy, resulting in the spin-flop transition. These results provide a comprehensive mechanism of interplay between spin, orbital, and lattice degrees of freedom to realize a low-field giant magnetoelasticity.

PACS numbers: 75.80.+q, 78.70.Ck, 78.70.Dm, 71.70.Ej

I. INTRODUCTION

Magnetoelasticity, coupling between magnetization and lattice strain, stems from a coupling between magnetic spin axis in an internal coordinate and lattice structure in a real coordinate through the relativistic spin-orbit coupling[1]. Recently, the magnetostriction is utilized for actuator, motor, and magnetostrictive sensor in future micro-mechanic devices[2]. In a ferromagnet, an external magnetic field induces only small magnetostriction ($\Delta L/L$) by rotating magnetic domains while the spin-orbit coupling often drives relatively large magnetostriction, and $\Delta L/L$ is enhanced even by two order of magnitude in rare-earth ($4f$) based magnetostrictive materials with the large spin-orbit coupling constant[1,3]. Terfenol-D ($Tb_{0.27}Dy_{0.73}Fe_2$) is one of the magnetostrive materials with the largest $\Delta L(H)/L$, in which the magnetic easy axis reorientates from the $\langle 111 \rangle$ to $\langle 100 \rangle$ direction resulting in strong magnetostrictive behaviors[1]. It is because the $4f$ wavefunction under the crystal field is tightly coupled with the magnetic axis.

On the other hand, $3d$ manganites suggest an alternative route to design giant magnetostriction materials with relatively small spin-orbit coupling constant. The system exhibits complex electrical and magnetic phase diagrams as a function of doping, temperature, and even external fields, and crossing over the phase boundaries evokes the emerging phenomena involving the interplay of the charge-spin-orbital-lattice degrees of freedom[5–7] . In this context, bilayer manganites $La_{2-2x}Sr_{1+2x}Mn_2O_7$ have attracted much attention due to not only the colossal magnetoresistance (CMR) phenomena[6–8] but also various intriguing features such as a polaronic metallic state[9], a photo-induced spin dynamics[10], and unusual charge/spin/orbital ordering behaviors[11–13]. $La_{1.4}Sr_{1.6}Mn_2O_7$, one of the CMR bilayered manganites, exhibits a noticeble magnetostrictive behavior. As presented in Fig. 1(a), its crystal structure consists of magnetic MnO_2 bilayers separated by a (La,Sr)O layer, and the magnetic structure exhibits consecutive ordering behaviors of antiferromagnetic (AFM) and ferromagnetic (FM) spin orders upon cooling through $T_N \simeq 100$ K and $T_C \simeq 75$ K, respectively. Upon heating across T_C, the inter-bilayer coupling switches from FM to AFM while the FM coupling within the bilayer remains and the system gets into an A-type AFM phase. The spin axis is mainly along the c-axis in both phases[6,8,14]. The magnetic switching is observable in the susceptibility (M/H) with varying temperature as shown in Fig. 1(b). M/H exhibits two anomalies around T_C and T_N, which are more distinguishable in the derivative shown in the inset. This AFM to FM switching leads an insulator-metal transition with two orders of magnitude resistivity reduction. This transition can be also driven by an external magnetic field just above T_C to yield CMR[8,15]. In addition, as shown in Fig. 1(c), the system exhibits huge magnetostriction of $\Delta L_c/L_c \sim 1.2 \times 10^{-3}$ at 2 T in the A-AFM phase[16], and its magnitude is even comparable to the large value of the magnetostrictive materials such as RCo_5 and RFe_2 (R = rare earth) obtained at low temperature (4 K) with a higher magnetic field ($H > 6$ T)[1,3].

In this paper, we studied a giant magnetostrictive spin-flop transition in $La_{1.4}Sr_{1.6}Mn_2O_7$ at low in-plane magnetic field ($\sim$ 0.1 T). The spin and orbital states were investigated by using resonant soft x-ray scattering

(RSXS) and x-ray absorption spectroscopy (XAS) at Mn $L_{2,3}$-edges. The RSXS results manifest the magntic-field driven spin-flop transition. A magnetic anisotropy switch plays a crucial role to trigger this transition, accompanying a certain change in the orbital occupation together with the magnetostrictive lattice distortion. Using theoretical configuration interaction (CI) model calculations, we demonstrated that this low-field giant magnetostrictive spin-flop is driven by a magnetocrystalline instability near a balanced occupation in $d_{x^2-y^2}$ and $d_{3z^2-r^2}$.

II. EXPERIMENT

High quality $La_{1.4}Sr_{1.6}Mn_2O_7$ single crystals were grown by a floating zone method. The magnetization were obtained by using a commercial magnetic property measurement system. The crystal exhibits consecutive magnetic transitions (see Fig. 1(b)) as in the previous reports[8,14]. The RSXS and XAS measurements were performed at 2A beamline in Pohang Light Source. A clean and shiny $(00L)$ surface was prepared by cleaving *in situ* of a vacuum better than 5×10^{-10} Torr. The RSXS intensity was obtained for the σ and π polarization geometries[17], and an electromagnet was synchronized with the sample rotation to keep the magnetic field along the a-axis as depicted in Fig. 2(a). The measurements were performed with cooling and heating from 78 K. The XAS intensity was measured in the total electron yield mode at 70° incident angle to the c-axis with planarly and vertically polarized light so that we could respectively obtained $E \parallel c$ and E⊥c spectra without changing the experimental geometry. The planar polarization with the 70° angle yields $\sim$ 90 % of the $E \parallel c$ absorption. The degree of linear polarization was better than 98 % for both polarizations. Many-body cluster model CI calculations (code XTLS 9.0)[18] were performed for a MnO_6 octahedron including the O $2p$ to Mn $3d$ charge transfer effects, the Mn $3d$ $L \cdot S$ coupling, full atomic multiplets, and the tetragonal distortion for different spin axes z (out-of-plane c) and x (in-plane a).

III. RESULTS AND DISCUSSIONS

A. Field Induced Spin-flop Transition

Figure 2(b) displays the RSXS scans along the $(00L)$ direction at $T = 78$ K. It shows a sharp $q = (001)$ Bragg forbidden reflection peak representing the A-AFM order. The fixed $q = (001)$ energy scan presented in Fig. 2(c) displays identical line shape for the σ- and π-polarization. The AFM order parameter, which is obtained from the integrated area, was monitored as a function of temperature shown in Fig. 2(d). Upon heating above 80 K, the order parameter decreases and disappears at $T_N \simeq 100$ K. It also decreases upon cooling below $T_C \simeq 75$ K due to development of FM domains[11,14]. Neutron studies reported that the low temperature FM phase has a canted FM order with an in-plane AFM one[14,19]. The remnant AFM order parameter at 20 K was estimated to be ~ 15 %, it indicating that some portion of A-AFM domain sustains below T_C with the phase competition. Despite large changes in both intensities I_σ and I_π with temperature, the ratio keeps a constant value $I_\sigma/I_\pi \simeq 0.86$ (see the inset in Fig. 2(d)), which corresponds to the spin axis 20° tilted from the c-axis, consistently with the previous results[8,14].

We performed the RSXS measurements under $H \parallel a$ to explore how the AFM order is affected by the field. Figure 3(a) shows the field dependent (001) AFM peak intensities I_σ and I_π. In the ac scattering plane for the θ - 2θ reflection (see Fig. 2(a)), the intensities are given by $I_\sigma = m_a^2 cos^2\theta + m_c^2 sin^2\theta$ and $I_\pi = m_a^2 cos^2\theta + m_c^2 sin^2\theta + 4m_b^2 sin^2\theta cos^2\theta$, where m_a, m_b, and m_c denote the a-, b-, and c-axis components of the local spin moments, respectively[20]. Here the scattering angle $2\theta \simeq 57°$ at $h\nu = 643$ eV, and I_σ and I_π are only attributed to the AFM components. At $H = 0$ ('A'), I_σ and I_π are maximized with $I_\sigma/I_\pi \simeq 0.86$ and $I_\pi - I_\sigma$ is finite with non-vanishing m_b due to the spin axis tilting. There is no crystalographic distinction between the a- and b-axis, and thus m_a should be equal to m_b at $H = 0$ (average over the magnetic domains). As H along the a-axis increases, I_σ abruptly drops at $H_C \simeq 540$ Oe while I_π gradually decreases with small kink features at $\pm H_C$ and $I_\pi - I_\sigma$ increases. At $H \sim 1,000$ Oe ('B'), I_σ vanishes, meaning that $m_a = 0$ and $m_c = 0$ in the AFM component and $I_\pi - I_\sigma$ becomes maximized (maximum m_b). It indicates that the spin axis of the AFM component flops from the nearly c- to b-axis.

In order to extract the spin components changing across the spin reorientation transition (SRT), three distinguishable AFM domains with spin components are counted in the simulation as follows;

$$(ac)\text{−AFM} : (m_a^{\mathrm{AC}}, m_c^{\mathrm{AC}}),$$
$$(bc)\text{−AFM} : (m_b^{\mathrm{BC}}, m_c^{\mathrm{BC}}),$$
$$(b)\text{−AFM} : (m_b^{\mathrm{B}}).$$

As the H-field is applied along the a-axis, the spins tend to tilt toward the filed direction, and thus an additional FM component (m_a^{FM}) is taken into account. The m_a^{FM} is determined from the in-plane M-H curve obtained from the SQUID measurement (see Supplementary Fig. S1). The total spin moment is set to be the nominal saturated magnetization 7.4 μ_B/f.u.. At $H = 0$, the spins are in the AFM order with the spin axis 20° tilted from the c-axis in either the ac- or bc-plane. There only exist (ac)- and (bc)-AFM domains with populations $p^{(ac)} = p^{(bc)} = 0.5$ and m_a and m_b contribution is same. It means that m_a^{AC} and m_c^{AC} in the (ac)-AFM domain and m_b^{BC} and m_c^{BC} in the (bc)-AFM domain equally contribute to the scattering intensities with $m_a^{\mathrm{AC}} = m_b^{\mathrm{BC}}$. When the applied field H along the a-axis increases, it is expected that the (ac)-

and (bc)-domain populations change unevenly and the additional $m_a^{\rm FM}$ along the field direction is turned on. At $H > 1500$ Oe, I_σ becomes zero. It means that $m_a^{\rm AFM} = m_c^{\rm AFM} = 0$ and thus both the (ac)- and (bc)-AFM domain populations vanish, i.e. $p^{(ac)} = p^{(bc)} = 0$ (see Fig. 3(c)). Now we have only canted (b)-AFM domains with $m_b^{\rm AFM}$ $(= m_b^{\rm B})$ and $m_a^{\rm FM}$ components.

Under the constraints described above, we simulated the measured intensity and determined ordered magnetic components as displayed in Fig. 3(b,c). Before the spin flop transition, the H-field partially switches the (ac)-AFM domain into the (bc)-AFM domain with sustaining the AFM easy axis on c-axis. Near the critical field, the net ordered $m_a^{\rm AFM}$ and $m_c^{\rm AFM}$ rapidly drop and finally become zero while $m_b^{\rm AFM}$ increases to keep the value of I_π, resulting from the spin flop transition from the (ac, bc)-AFM to the (b)-AFM order. After the spin flop transition, $m_b^{\rm AFM}$ gradually decreases with increase of $m_a^{\rm FM}$ due to the magnetic field and becomes saturated at $H \sim 4000$ Oe (see Supplementary Fig. S1), consistently with the I_π behavior. One can notice certain reduction in the ordered total net moment near the spin-flop transition, indicating that the competition between (ac, bc)-AFM and (b)-AFM orderings causes a certain degree of disorder in the AFM components at the domain boundaries.

Figure 4 presents two-dimensional maps of $I_{\sigma,\pi}$ versus temperature and applied H-field, obtained by accumulating the H-field dependences (see Fig. 3(a)) at different temperatures. The spin-flop crossover is clearly observable in $|\partial I_{\sigma,\pi}/\partial H|$, both of which expose prominent maxima around $H_C \simeq 540$ Oe in the A-AFM window (75 K $\leq T \leq 100$ K), as shown in Fig. 4(c,d). The spin structures before and after the spin flop transition are schematically depicted in Fig. 4(c). In the AFM phase, the ordered spin is aligned mostly along the c-axis at $H = 0$[14,15]. As H increases, the spin axis flops around H_C and the spin axis lies in the ab plane with both FM m_a and AFM m_b. In the low temperature FM phase, the FM spins are also aligned along the near c-axis at $H = 0$ and gradually turn to the H-field direction to become fully along the a-axis at $H > 6000$ Oe with the saturated magnetization.

B. Magnetostriction and Magnetocrystalline Anisotropy

The RSXS study manifests the spin-flop transition induced by the H-field in $La_{1.4}Sr_{1.6}Mn_2O_7$. The spin-flop accompanies a giant magnetoelastic response with c-axis contraction and ab-plane expansion[16], implying a certain change in the orbital state. The system consists of Mn^{3+} $(t_{2g}^3 e_g^1)$ and Mn^{4+} (t_{2g}^3) with a $7:3$ ratio. The doubly degenerated e_g state naturally gives an orbital degree of freedom of the in-plane $d_{x^2-y^2}$ and out of-plane $d_{3z^2-r^2}$ for the additional e_g electron in Mn^{3+}. Thus we examined the orbital character using the Mn $L_{2,3}$-edge $(2p \rightarrow 3d)$ polarization dependent ($E \perp c$ and $E \parallel c$) XAS. Figure 5(a) displays the L_2-edge spectra for various temperatures with and without the in-plane $H \simeq 3500$ Oe. All the spectra exhibit certain polarization dependence, indicating that there exists anisotropy in the e_g orbital occupation (Supplemental Fig. S2 for the entire $L_{2,3}$ region).

The polarization dependence can be seen more clearly in the linear dichroism (LD), the difference spectrum ($E \perp c - E \parallel c$), as shown in Fig. 5(b). The $L_{2,3}$-edge LD spectra exhibit rather complicated line shapes, but a prominent change appears near the threshold, which corresponds to the lowest energy transition Mn^{3+} $t_{2g}^3 e_g^1(^5E) \rightarrow \underline{2p}\ t_{2g}^3 e_g^2(^6A_1)$ with a $2p$ core hole. Due to the dipole selection rule, the $E \parallel c$ and $E \perp c$ polarizations emphasize the transition to $d_{x^2-y^2}$ and $d_{3z^2-r^2}$ holes, respectively. This LD signal is positive at $T = 80$ K (AFM phase) but becomes negative at $T = 20$ K (FM phase). These results tell us that the $d_{3z^2-r^2}$ occupation dominate over the $d_{x^2-y^2}$ one in the AFM phase but it becomes opposite in the FM phase.

Indeed, it is confirmed in the theoretical many-body configuration interaction (CI) calculations for the LD spectra in which this sign inversion occurs with the change in the occupied orbital from $d_{3z^2-r^2}$ to $d_{x^2-y^2}$. The calculations reproduce the overall LD line shapes for both orbital occupation cases as displayed in Fig. 5(c,d). The CI calculations were performed by using XTLS9.0 code[18]. In the CI calculation, we took into account the tetragonal (D_{4h}) crystal field, a Mn $3d$ − O $2p$ hybridization, and full atomic multiplets driven by Mn $3d - 3d$ and Mn $2p - 3d$ Coulomb interactions. To mimic the LD spectra $La_{1.4}Sr_{1.6}Mn_2O_7$ ($x = 0.3$), we applied the $7:3$ weighted average of Mn^{3+} and Mn^{4+} in the spectra. The occupied e_g orbital in Mn^{3+} was selected by tuning the tetragonal distortion, i.e. elongation or compression of MnO_6 octahedron for the $d_{3z^2-r^2}$ or $d_{x^2-y^2}$ orbital occupation, respectively. For Mn^{4+}, a small tetragonal distortion (elongation) reflecting the layered structure is commonly applied in both calculated LD spectra in order to capture the wider band width of $d_{x^2-y^2}$ resulting positive LD at the tail of each $L_{2,3}$-edge. The CI calculations definitely show the sign inversion of LD at the leading edge of the $L_{3,2}$-edges with certain change in the e_g orbital occupation. Besides the sign inversion of the leading edge feature, the overall features of the observed LD spectra are also well reproduced in the calculated ones.

At 60 K, the threshold LD signal is still positive, but is significantly reduced. The reason is that the system is still dominated by the AFM phase although the FM phase partially develops below $T_C \simeq 75$ K. Upon cooling across the AFM-FM transition, the c lattice constant contracts significantly while the ab ones expand[16]. Compression of the MnO_6 cage along the c-axis[11] makes partial transfer of the occupied $d_{3z^2-r^2}$ electrons into the $d_{x^2-y^2}$ states. This orbital occupation change is also driven by the in-plane H-field. The LD line shape switches again in the magnetic field at $T = 80$ K (also at

$T = 60$ K) as shown in the right panel in the figure. These results manifests that the giant magnetoelasticity in the AFM phase is induced by switching the dominant occupied orbital from $d_{3z^2-r^2}$ to $d_{x^2-y^2}$ accompanied with the spin-flop transition involving a change of the magnetocrystalline anisotropy (MCA).

In order to understand microscopic mechanism of the magnetoelasticity, we explore how the lattice distortion affects the orbital occupation and MCA. The many-body cluster model model calculation is performed for Mn^{3+} (d^4) in an MnO_6 octahedron with a variation of the tetrahedral distortion $\Delta c/c$, the elongation ratio of Mn-O (apical) distance along the c-axis. Figure 6(a) shows the calculation results for the $d_{x^2-y^2}$ and $d_{3z^2-r^2}$ occupations for two different spin axes. The positive (negative) $\Delta c/c$ represents an elongated (compressed) octahedron. The occupation number $n_{x^2-y^2}$ and $n_{3z^2-r^2}$ vary with $\Delta c/c$ although their sum is nearly constant. Interestingly, as the spin lies along the z-axis (x-axis), the $L \cdot S$ coupling effectively lowers the $d_{3z^2-r^2}$ ($d_{x^2-y^2}$) energy to increase $n_{3z^2-r^2}$ ($n_{x^2-y^2}$) slightly and contributes positive $\Delta L = L_z - L_x$ (negative ΔL) even for $\Delta c/c = 0$, in which $n_{3z^2-r^2} = n_{x^2-y^2}$ and $L_{x,y} = L_z = 0$ without the $L \cdot S$ coupling (Supplemental Fig. S3). This result shows that the $L \cdot S$ coupling lowers the system energy by inducing and unquenched orbital moment even in the perfect octahedron. In the second order perturbation theory of the $L \cdot S$ coupling for the Mn^{3+} ion in the crystal field, the orbital moments are estimated to be $L_x = 3n_{x^2-y^2}\zeta_{3d}/10Dq$ and $L_z = 4n_{3z^2-r^2}\zeta_{3d}/10Dq$ with the Mn $3d$ spin-orbit coupling constant $\zeta_{3d}^{\rm Mn}$ ($\simeq$ 0.045 eV), and the crystal field splitting $10Dq$[24]. Supposed $10Dq = 1.5$ eV, the unqueched moment is estimated to be $L_x = 0.09$ ($L_z = 0.12$) for the unoccupied hole number $n_{x^2-y^2}$ ($n_{3z^2-r^2}$) $= 1$. These ionic orbital moment values are redueced by the covalency and partial orbital occupations in the MnO_6 with Mn $3d$-O $2p$ hybridization as in Fig. 6(b).

The MCA energy is defined by the energy difference of the $L \cdot S$ coupling as the spins are aligned along the a-axis (S_x) and c-axis (S_z), and thus is determined by L_z with the spin axis c and L_x with the spin axis a. Figure 6(b) shows the corresponding L_x and L_z calculated as a function of $\Delta c/c$. For the elongation (compression), $\Delta c/c > 0$ ($\Delta c/c < 0$), the e_g occupation is dominated by $d_{3z^2-r^2}$ ($d_{x^2-y^2}$) and ΔL becomes positive (negative). This occupation imbalance gives rise to the anisotropy of unquenched orbital moments. These results strongly suggest instability in MCA very near a critical e_g configuration of $n_{3z^2-r^2} \simeq n_{x^2-y^2}$ in manganites with Mn^{3+}, where the spin axis cooperates with the tetragonal distortion for the e_g occupation change. This instability drives a giant magnetoelastic spin-flop transition in $La_{1.4}Sr_{1.6}Mn_2O_7$. When the c spin axis is forced to be turned by an in-plane H-field, $d_{3z^2-r^2}$ electrons are partially transferred into the $d_{x^2-y^2}$ state in order to minimize the energy cost of the $L \cdot S$ coupling. As the transferred electron becomes sufficiently large near H_C, the octahedron is compressed and ΔL switches the sign to flop the spin axis. At 80 K (AFM phase), we obtained $\Delta c(H)/c \simeq -450 \times 10^{-6}$ at $H = 3500$ Oe (Supplemental Fig. S4). This value is large enough to switch the dominant orbital and the sign of ΔL (MCA). In the FM metallic phase (20 K), $n_{x^2-y^2}$ becomes larger than $n_{3z^2-r^2}$ due to the compressed octahedron, but the spin axis remains along the c-axis. It is likely due to orbital momentum quenching of the in-plane conducting electrons. The H-filed increases $n_{x^2-y^2}$ further to flop the spin axis to lie in the plane.

IV. DISCUSSION AND CONCLUSION

Switching of the magnetic easy axis can be induced by fine tuning of doping, pressure, strain, and external fields due to intimate coupling of spin, orbital, and lattice degrees of freedom. In $La_{2-2x}Sr_{1+2x}Mn_2O_7$, the magnetic axis, which is along the c-axis at $x \leq 0.32$, switches into the in-plane direction at $x \geq 0.33$, in which the c lattice parameter is reduced[10,11] and $n_{3z^2-r^2}$ relatively decreases while the direction of magnetic anisotropy changes from the c-axis to the ab-plane[25]. At $x \simeq 0.32$, the spin axis switches even through photoexcitations[10]. Indeed, the similar relation between structure and magnetic anisotropy is also validated for $La_{1-x}Sr_{1+x}MnO_4$[26], in which the e_g orbital occupation changes by transfering $d_{3z^2-r^2}$ electrons to $d_{x^2-y^2}$ orbital[27,28]. The magnetic axis tuning was also demonstrated in $La_{0.7}Ca_{0.3}MnO_3$ epitaxial films, in which MCA can be controlled through strain engineering[29]. In $La_{1.4}Sr_{1.6}Mn_2O_7$ ($x = 0.3$), the external magnetic field trrigers to change the spin axis, and the $L \cdot S$ coupling leads a change in the e_g occupation accompanied with the compressive lattice distortion, resulting in the giant magnetoelastic spin-flop at a low H-field (< 0.1 T). These results illuminate the comprehensive mechanism for a low field giant magnetoelasticity induced by the magnetocrystalline instability and suggest us a route to design new magnetostrictive materials based on the transition metal oxides.

In summary, we investigated a giant magnetoelastic spin-flop transition of a CMR manganite $La_{1.4}Sr_{1.6}Mn_2O_7$ in presence of in-plane H-fields. The detailed examinations of spin and orbital states demonstrate that the transition is driven by magnetocrystalline instabilty near a critical orbital occupation. Due to the instability, a small field flopping of the magnetic axis leads a certain change in the orbital occupation due to the spin-orbit coupling. This change accompanies lattice distortion and magnetic anisotropy switching, resulting in the magnetostrictive spin-flop transition.

This work is supported by Study for Nano Scale Optomaterials and Complex Phase Materials (2016K1A4A4A01922028) through NRF funded by MSIP of Korea. PAL is supported by MSIP of Korea.

* Kyung-Tae.Ko@mpk.or.kr
† jhp@postech.ac.kr

[1] P. Morin, and D. Schmitt, in *Ferromagnetic Materials* edited by K. H. J. Buschow and E. P. Wohlfarth (Elsevier, 1990), p. 1.
[2] A.G. Olabi, and A. Grunwald, Materials and Design **29**, 469 (2008).
[3] A. E. Clark, and H. S. Belson, Phys. Rev. B **5**, 3642 (1972).
[4] A. E. Clack, J. P. Teter, and M. Wun-Fogle, J. Appl. Phys. **69**, 5771 (1991).
[5] Y, Tokura, Rep. Prog. Phys. **69**, 797 (2006).
[6] T. Kimura, and Y. Tokura, Annu. Rev. Mater. Sci. **30**, 451 (2000).
[7] J. F. Mitchell, D. N. Argyriou, A. Berger, K. E. Gray, R. Osborn, and U. Welp, J. Phys. Chem. **105**, 10731 (2001).
[8] T. Kimura, Y. Tomioka, H. Kuwahara, A. Asamitsu, M. Tamura, and Y. Tokura, Science **274**, 1698 (1996).
[9] F. Weber, N. Aliouane, H. Zheng, J. F. Mitchell, D. N. Argyriou, and D. Reznik, Nature Mat. **8**, 798 (2009).
[10] S. Tomimoto, M. Matsubara, T. Ogasawara, H. Okamoto, T. Kimura, and Y. Tokura, Phys. Rev. Lett. **98**, 017402 (2007).
[11] Masato Kubota, Hirofumi Fujioka, Kazuma Hirota, Kenji Ohoyama, Yutaka Moritomo, Hideki Yoshizawa, and Yasuo Endoh, J. Phys. Soc. Jpn. **69**, 1606 (2000).
[12] Qing'An Li, K. E. Gray, H. Zheng, H. Claus, S. Rosenkranz, S. N. Ancona, R. Osborn, J. F. Mitchell, Y. Chen, and J. W. Lynn, Phys. Rev. Lett. **98**, 167201 (2007).
[13] J.-S. Lee, C.-C. Kao, C. S. Nelson, H. Jang, K.-T. Ko, S. B. Kim, Y. J. Choi, S.-W. Cheong, S. Smadici, P. Abbamonte, and J.-H. Park, Phys. Rev. Lett. **107**, 037206 (2011).
[14] K. V. Kamenev, G. J. McIntyre, Z. Arnold, J. Kamarád, M. R. Lees, G. Balakrishnan, E. M. L. Chung, and D. McK. Paul, Phys. Rev. Lett. **87**, 167203 (2001).
[15] T. G. Perring, G. Aeppli, T. Kimura, Y. Tokura, and M. A. Adams, Phys. Rev. B **58**, 14693(R) (1998).
[16] T. Kimura, Y. Tomioka, A. Asamitsu, and Y. Tokura, Phys. Rev. Lett. **81**, 5920 (1998).
[17] J.-S. Lee, B. H. Seung, T.-Y. Khim, H. Jang, K.-T. Ko, B.-G. Park, J.-H. Park, K.-B. Lee, and J.-Y. Kim, J. Kor. Phys. Soc. **52**, 1814 (2008).
[18] A. Tanaka, and T. Jo, J. Phys. Soc. Jpn. **63**, 2788 (1994).
[19] D. N. Argyriou, J. F. Mitchell, P. G. Radaelli, H. N. Bordallo, D. E. Cox, M. Medarde, and J. D. Jorgensen, Phys. Rev. B **59**, 8695 (1999).
[20] Hoyoung Jang, J.-S. Lee, K.-T. Ko, W.-S. Noh, T. Y. Koo, J.-Y. Kim, K.-B. Lee, J.-H. Park, C. L. Zhang, Sung Baek Kim, and S.-W. Cheong, Phys. Rev. Lett. **106**, 047203 (2011).
[21] D. Louca, G. H. Kwei, and J. F. Mitchell, Phys. Rev. Lett. **80**, 3811 (1998).
[22] T. Ishikawa, K. Tobe, T. Kimura, T. Katsufuji, and Y. Tokura, Phys. Rev. B **62**, 12354 (2000).
[23] R. H. Heffner, D. E. MacLaughlin, G. J. Nieuwenhuys, T. Kimura, G. M. Luke, Y. Tokura, and Y. J. Uemura, Phys. Rev. Lett. **81**, 1706 (1998).
[24] J. Stöhr, and H. König, Phys. Rev. Lett. **75**, 3748 (1995).
[25] R. Saniz, M. R. Norman, and A. J. Freeman, Phys. Rev. Lett. **101**, 236402 (2008).
[26] S. Larochelle, A. Mehta, L. Lu, P. K. Mang, O. P. Vajk, N. Kaneko, J. W. Lynn, L. Zhou, and M. Greven, Phys. Rev. B **71**, 024435 (2005).
[27] D. J. Huang, W. B. Wu, G. Y. Guo, H.-J. Lin, T. Y. Hou, C. F. Chang, C. T. Chen, A. Fujimori, T. Kimura, H. B. Huang, A. Tanaka, and T. Jo, Phys. Rev. Lett. **92**, 087202 (2004).
[28] Hua Wu, C. F. Chang, O. Schumann, Z. Hu, J. C. Cezar, T. Burnus, N. Hollmann, N. B. Brookes, A. Tanaka, M. Braden, L. H. Tjeng, and D. I. Khomskii, Phys. Rev. B **84**, 155126 (2011).
[29] J. H. Song, J.-H. Park, J.-Y. Kim, B.-G. Park, Y. H. Jeong, H.-J. Noh, S.-J. Oh, H.-J. Lin, and C. T. Chen, Phys. Rev. B **72**, 060405(R) (2005).

FIGURES

FIG. 1. (color online) (a) Crystal and spin structures of $La_{1.4}Sr_{1.6}Mn_2O_7$. (b) Zero field cooled M vs. T curve ($H \parallel c$). Two consecutive magnetic transitions are indicated by blue arrows. Its derivative is presented in the inset. (c) Schematic drawing of the magnetoelastic response to an in-plane magnetic field.

FIG. 2. (color online) (a) RSXS experimental geometry under the external H-field along the a-axis. (b) $(00L)$ scans of $La_{1.4}Sr_{1.6}Mn_2O_7$ at $H = 0$ Oe for both σ and π polarizations. (c) (001) fixed q energy spectra at Mn $L_{2,3}$-edges. (d) Temperature dependent A-AFM order parameters obtained from the (001) peak areas of I_σ and I_π. The ratio I_σ/I_π is presented in the inset.

FIG. 3. (color online) (a) H-field dependent (001) A-AFM peak intensities I_σ and I_π maximized at $H = 0$ ('A'). (b) The intensities obtained from model calculations (solid lines) are compared with the experimental ones (open circles). (c) Estimated net spin AFM components (m_a, m_b, m_c) from the ordered (ac)-, (bc)-, and (b)-AFM domains with respective $(m_a^{\mathrm{AC}}, 0, m_c^{\mathrm{AC}})$ and $(0, m_b^{\mathrm{BC}}, m_c^{\mathrm{BC}})$, and $(0, m_b^{\mathrm{B}}, 0)$ AFM components. An additional FM component (m_a^{FM}) induced by the magnetic field $H \parallel a$ is taken into account for each AFM domain, and the net moment m_{FM} is also presented in the figure. The black triangle indicates the total ordered moment of which the nominal value at $H = 0$ is set to be $6.7\mu_B$/f.u.

FIG. 4. (color online).(a-b) H-field dependent (001) A-AFM intensity maps are displayed. The intensity is measured using π (blue) and σ (red) incident polarization. (c-d) $\left|\partial I_{(001)}/\partial H\right|$ intensity maps are displayed. The high intensity line near 540 Oe indicates the critical field of SRT. (e) Schematic spin configuration of each point is displayed.

FIG. 5. (color online) (a) Mn L_2-edge XAS spectra measured at 80 K, 60 K, and 20 K with and without an in-plane magnetic field ($H//a$ = 3500 Oe). The spectra obtained at the E $\parallel$ c and E $\perp$ c polarization geometries are presented with blue and red solid lines, respectively. (b) Corresponding LD spectra of Mn $L_{2,3}$-edges. (c) CI model calculation LD spectrum for the elongated Mn^{3+} compared with the 80 K experimental one. (d) CI model calculation LD spectrum for the compressed Mn^{3+} compared with the 20 K experimental one.

FIG. 6. (color online) (a) Calculated occupations of $d_{3z^2-r^2}$ and $d_{x^2-y^2}$ e_g orbitals of Mn^{3+} as a function of $\Delta c/c$, an elongation ratio of the Mn-apical oxygen (O_{ap}) distance, in an MnO_6 octahedron. Solid and dot-dashed lines present the $d_{3z^2-r^2}$ and $d_{x^2-y^2}$ orbital occupations, respectively. Due to the $L \cdot S$ coupling, the orbital occupations vary with the spin direction, along the a- (blue) or c-axis (red). (b) Calculated orbital angular momenta L_x with the spin axis a and L_z with the spin axis c, which determine the magnetocrystalline anisotropy (MCA), as a function of $\Delta c/c$. The $\Delta L = L_z - L_x$ changes the sign across $\Delta c/c = 0$, resulting in the MCA switch.

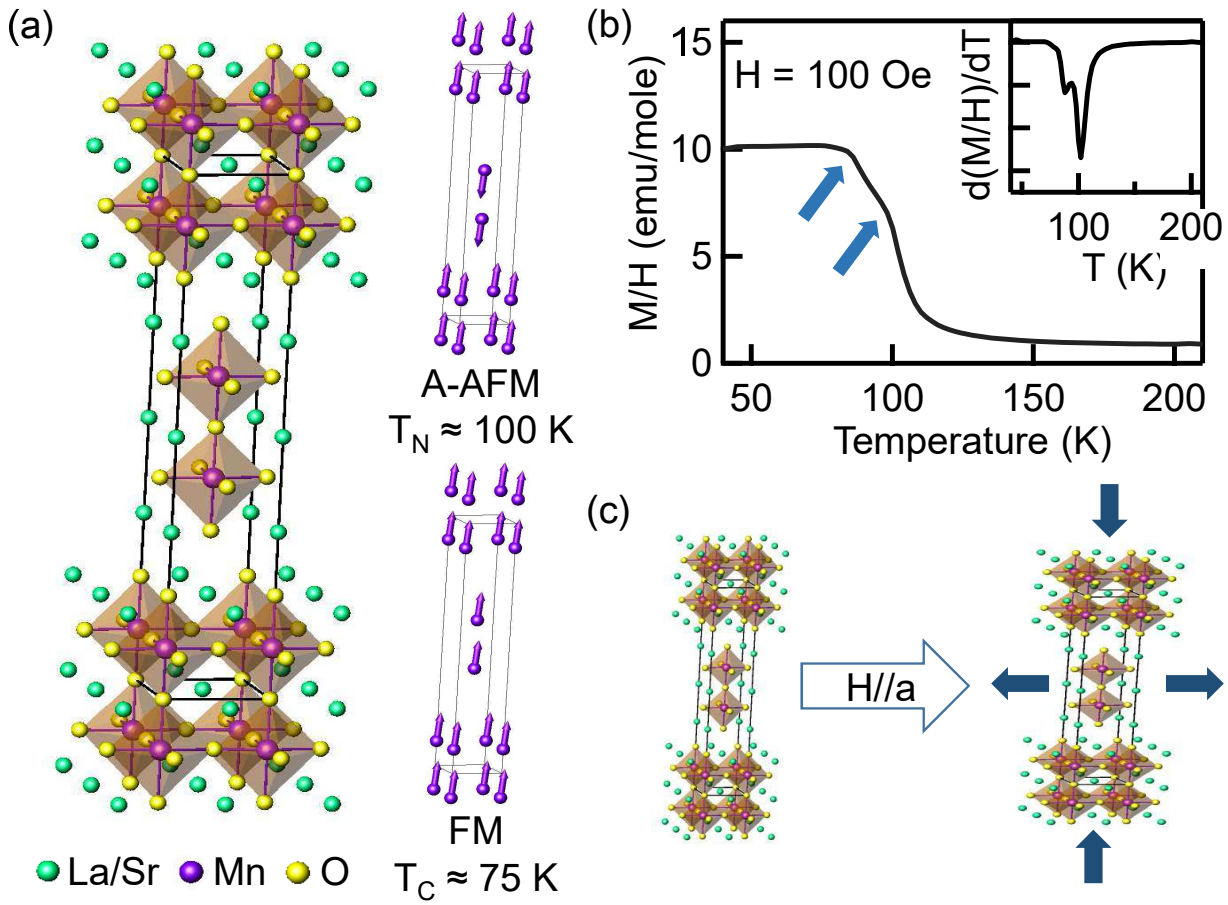

Figure 1 19Dec2017

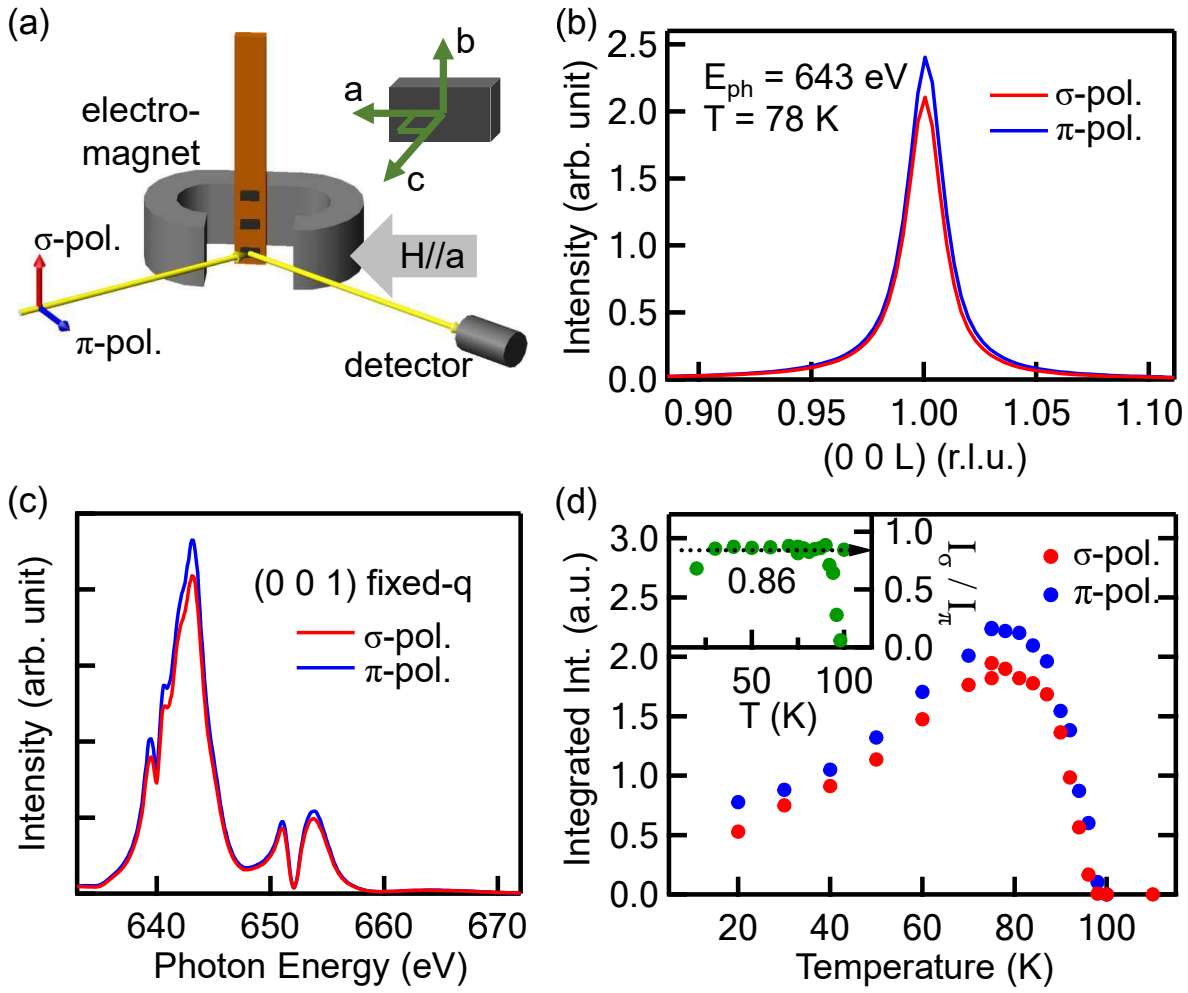

Figure 2 19Dec2017

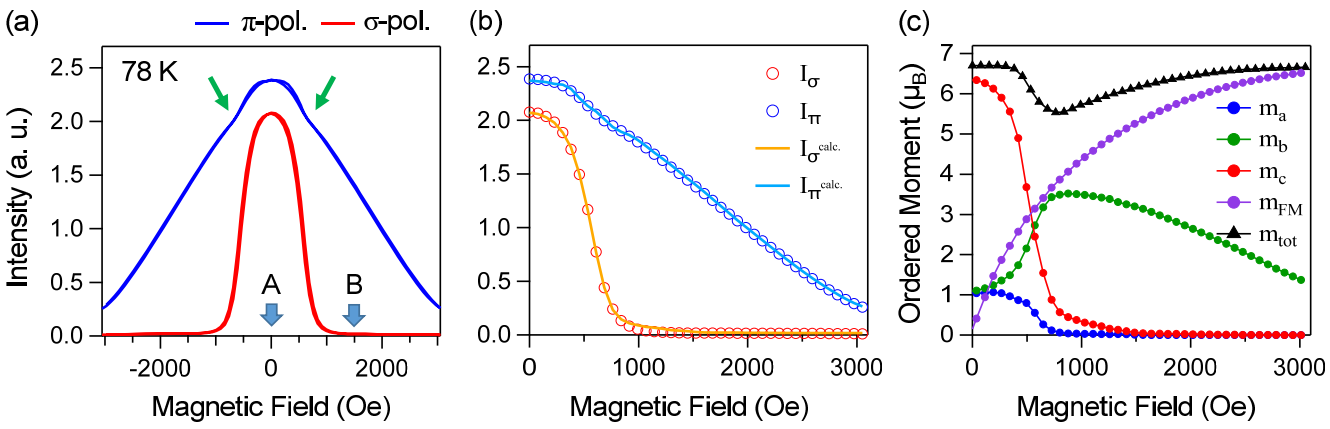

Figure 3 19Dec2017

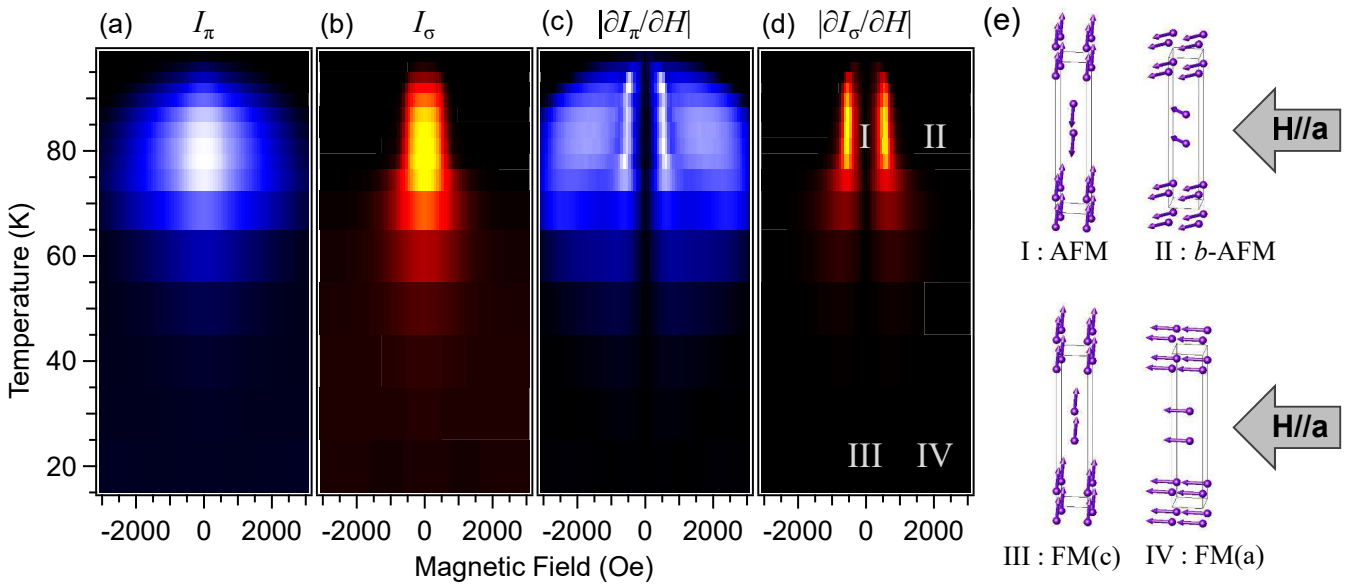

Figure 4 19Dec2017

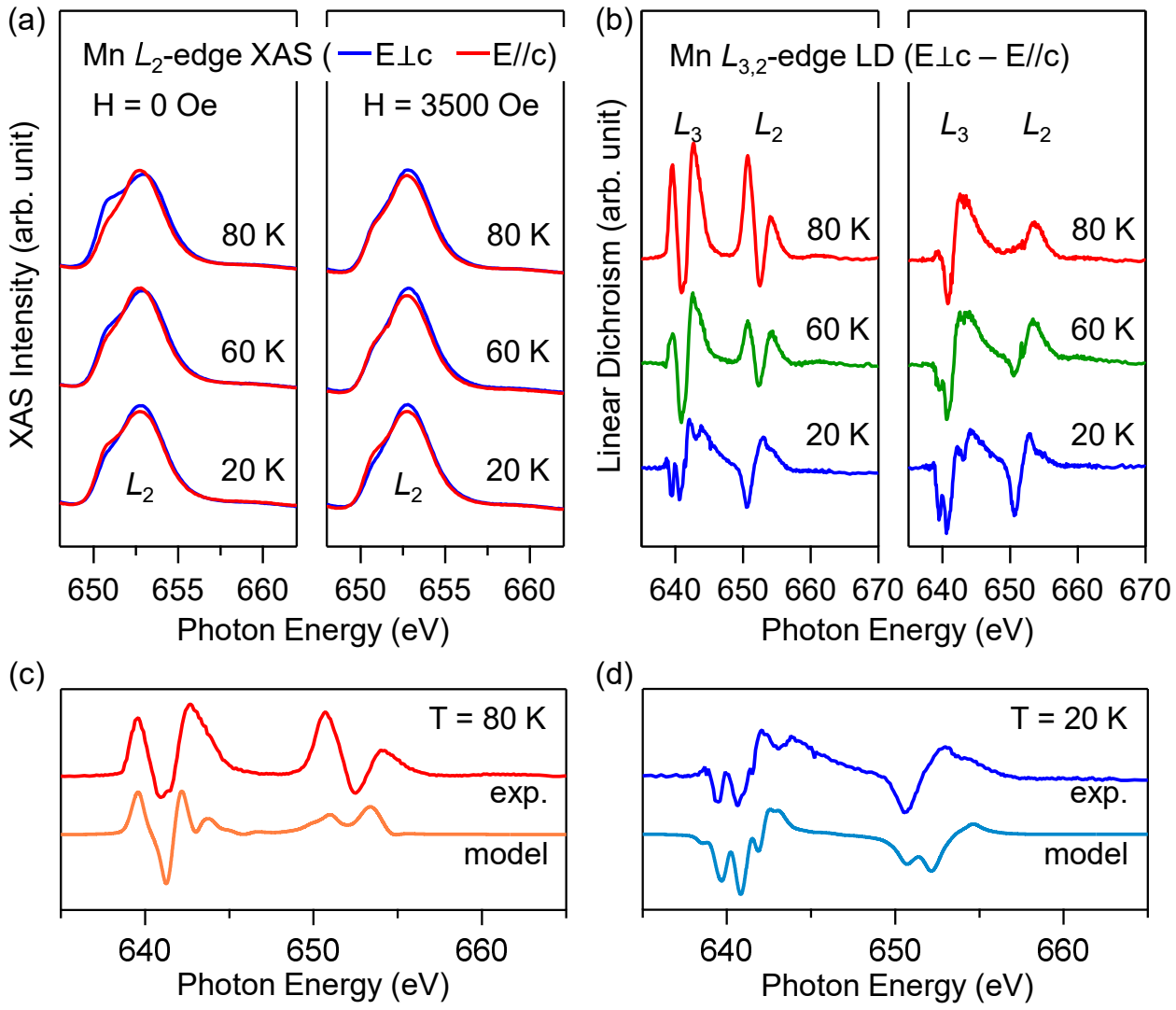

Figure 5 19Dec2017

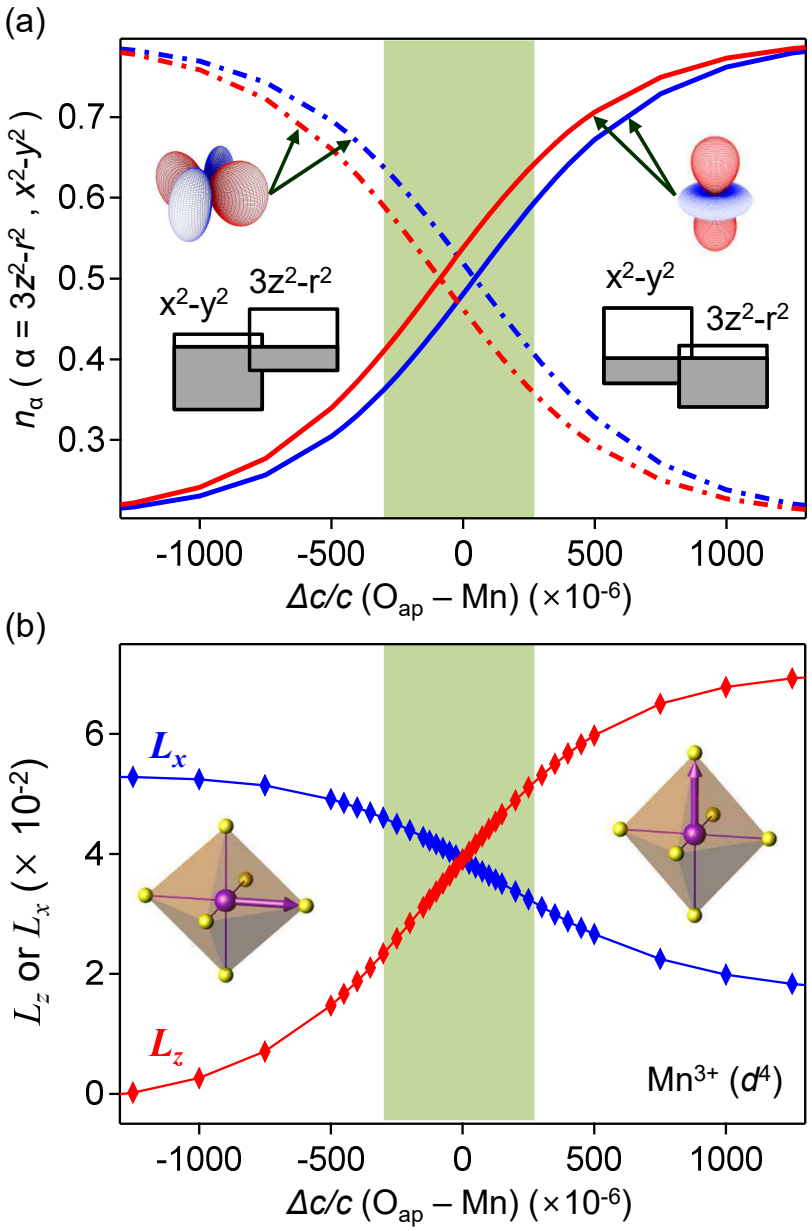

Figure 6 19Dec2017